# Numerical Study on Flame Stabilization and NO$_x$ Formation in a Novel Burner System for Sulfur Combustion

Feichi Zhang,* Maksymilian Kurjata, Nadia Sebbar, Thorsten Zirwes, Michal Fedoryk, Stefan Harth, Robert Wang, Peter Habisreuther, Dimosthenis Trimis, and Henning Bockhorn

**ABSTRACT:** Numerical simulations have been conducted for a novel double concentric swirl burner, which is specifically designed for combustion of sulfur with a high power density. The burner serves as a major component of an enclosed conversion cycle, which uses elemental sulfur as a carbon free chemical energy carrier for storing solar energy. The focus of the work is to assess operability of the burner and NO$_x$ formation at fuel lean conditions with an equivalence ratio of $\phi$ = 0.5, which is crucial regarding flame stabilization and evaporation. To quantitatively evaluate the NO$_x$ formation, a new reaction mechanism for sulfur combustion along with S/N/O and NO$_x$ reactions has been developed and used for the simulation. In comparison to our previous simulations using a higher $\phi$, the flame is lifted slightly and the overall flame temperature is lowered in the current case, leading to a weakened evaporation performance. Accordingly, an increased share of sulfur droplets hitting the chamber wall and escaping the domain has been confirmed. The local NO$_x$ share has been shown to increase strongly with the flame temperature from a threshold value of approximately 1600 K. In addition, the NO$_x$ formation from the burner setup with a high swirl intensity (HSI) has been shown to be 2 times higher than that with a low swirl intensity (LSI). This is attributed to a higher flame temperature and longer residence time caused by a strong inner recirculation flow. However, the HSI setup yields a better evaporation performance and a reinforced flame stabilization. The results reveal a trade off for operating the sulfur burner with different burner designs and equivalence ratios.
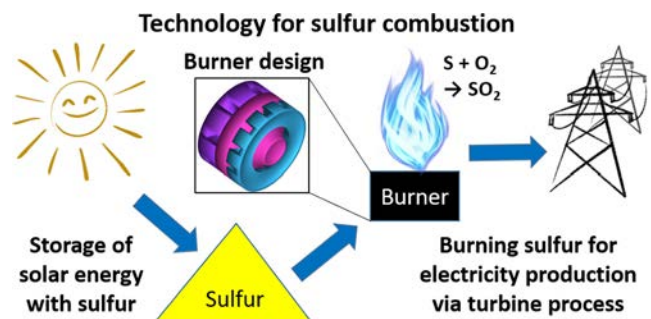
## INTRODUCTION

The worldwide energy generation is facing urgent environ mental and technological challenges in terms of carbon neutralization, which demands a transition of the energy infrastructure from utilization of fossil fuels to renewable energy sources. However, the power outputs from solar and wind energy, which represent the most important sources for renewable energy technologies, are subjected to strong time fluctuations or intermittency. To solve this problem, a key technology for the utilization of renewable energy is to store the excess renewably generated energy with chemical energy carriers through thermochemical processes. In this way, the generated renewable fuels enable the satisfaction of power demands at times of otherwise low energy generation. For example, the excess renewable power can be used to produce hydrogen by means of water electrolysis, which can be used to produce electricity in a fuel cell or for other chemical engineering processes, e.g., for the refinery industry or ammonia production. Therefore, a transition of the chemical energy carrier from fossil to renewable fuels will accompany the long term energy transition stage, and combustion will

remain as an essential technology for designing future flexible energy systems, employing a large variety of renewable fuels.

To generate electricity based on heat from the sun, one state of the art way is to use movable mirrors to track and focus the sunlight. The high temperature heat produced in this way can be converted into electrical power via a steam turbine process. In combination with a proper thermal energy storage system, such concentrated solar power (CSP) plants can continually provide electricity even after sundown. Molten salts are generally used in these CSP plants as sensible storage fluid of solar heat.[1,2,6] However, its maximum operating temperature is around 550 °C, which limits the process efficiency. In addition, the storage of molten salt is not suitable for long term application because heat stored in the medium will inevitably
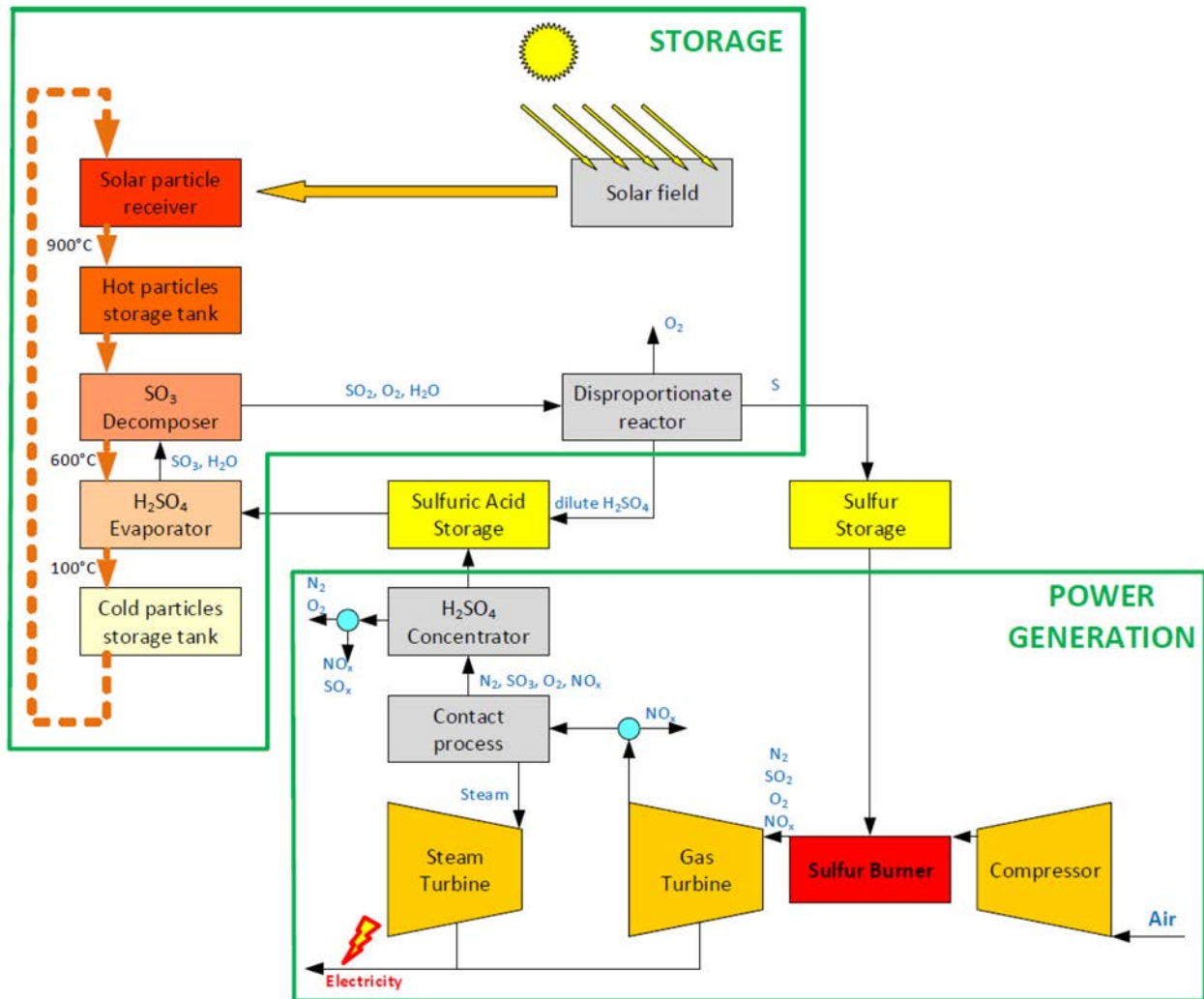
**Figure 1.** Process workflow of the sulfur based thermochemical cycle for storage and utilization of solar energy.

be lost to the environment.[3] For this reason, it cannot be used for seasonal storage.

To overcome these drawbacks, the European Commission (EC) funded PEGASUS project (Renewable Power Gener ation by Solar Particle Receiver Driven Sulfur Storage Cycle) has the overarching objective to demonstrate a baseload capable novel power cycle for the utilization of concentrated solar thermal energy with the help of sulfur as the chemical energy carrier.[3] In this process, elemental sulfur is used as a carbon free chemical carrier for storing solar heat, which can be burned in a gas turbine to produce electricity. As illustrated schematically in Figure 1, the whole cycle can be divided into two parts connected with each other: (1) decomposition of sulfuric acid into sulfur with the help of solar heat (upper part in Figure 1) and (2) combustion of sulfur and subsequent production of sulfuric acid and electricity (lower part in Figure 1).

In the solar thermal plant, sulfuric acid is evaporated and subsequently decomposed to sulfur dioxide, which is fed to the disproportionation reactor. The disproportionation reactor produces elemental sulfur, which can be easily stored as solid sulfur and continuously fed to the power generation process presented on the bottom of Figure 1. The sulfur burner is directly integrated into a gas turbine, and the heat of the exhaust gases is used by a steam turbine. The application of a

gas turbine operated with sulfur is favorable in terms of efficiency but challenging in terms of suitable construction materials and burner technology. The exhaust gases of the gas turbine are used to generate sulfuric acid, which is supplied again to the solar thermal plant.

$NO_x$ generated from sulfur combustion represents a known challenge in the sulfuric acid production. The presence of nitrates in the acid leads to faster corrosion of steel equipment and reduces the quality of the acid. Therefore, $NO_x$ or nitrogen compounds are intentionally kept as low as possible. According to this, one objective of the current work is to gain in depth knowledge for the formation process of $NO_x$ and to quantitatively assess the amount of $NO_x$ from sulfur combustion. For the sulfur−solar cycle, the separation of $NO_x$ by means of gas cleaning techniques takes place prior to the first catalyst pass (contact process), as indicated in Figure 1. A more detailed description of the overall process can be found in refs 3−5.

In comparison to state of the art CSP techniques, the storage capacity of sulfur is more than an order of magnitude higher than the sensible heat storage of molten salt (heating value of sulfur $H_S$ = 9.6 MJ/kg versus specific energy of 0.3 MJ/kg of molten salt). In addition, sulfur is a more cost effective material compared to molten salt. Moreover, sulfur can be cheaply stored for very long times and in huge amounts
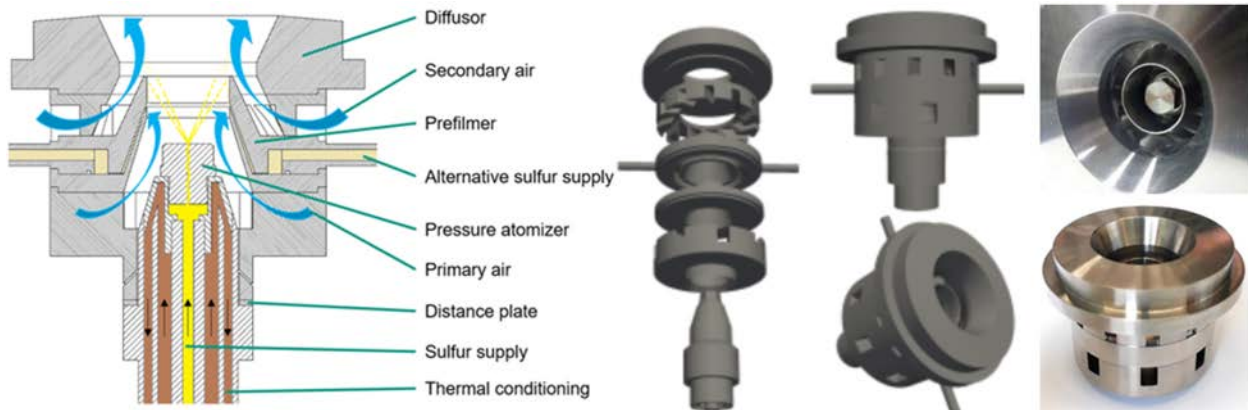
**Figure 2.** (Left) Cross section view and (right) exploited view of the burner nozzle developed for combustion of sulfur.

under ambient conditions. The resulting low specific storage costs together with the high energy density of sulfur contribute to a cheap and flexible use of solar energy resources. However, one drawback or difficulty in the proposed process is that a novel system for combustion of sulfur has to be designed. Additionally, the burner produces the toxic flue gas $SO_x$. The complex combustion behavior of sulfur in this context has not been studied before.

In this context, objective of the current project at the Karlsruhe Institute of Technology (KIT) is to develop a burner system for a detailed study of the combustion process of sulfur, which is suitable to be integrated into the proposed sulfur–solar energy storage system. Nowadays, however, applications of sulfur combustion are either used to produce sulfuric acid within large scale furnaces, or sulfur is burned together with fossil fuels as undesired trace substances. Hence, there are no existing burner concepts for the required high power density combustion of sulfur in terms of gas turbine applications. For this reason, a novel double concentric swirl burner has been developed,[4,5] which is capable of operation with a thermal load of up to 50 kW, yielding a power density of up to 5 MW/m$^3$ at ambient conditions. The general applicability of the burner has been justified in preliminary spray experiments and sulfur combustion simulations,[4,5,7] which provide a first insight into the combustion process of sulfur when using the designed burner. There, the simulations have been carried out for two nozzle configurations with high and low airflow swirl intensities (HSI versus LSI), and the performance of both nozzle setups has been assessed extensively with regard to their operability, burning efficiency, and flame stabilization.

The previous simulations in refs 5, 7, and 8 have reproduced the main characteristics of the governing flow field, spray dispersion, and flame stabilization. A strong inner recirculation zone (IRZ) was observed for the HSI nozzle, which leads to a broader and shorter flame compared to the LSI nozzle. The IRZ results in enhanced evaporation and mixing processes, so that the flame temperature in the HSI case is higher compared to the LSI burner. In addition, it has been shown that the LSI burner leads to less droplets hitting the chamber wall compared to the HSI case. This is beneficial with regard to preventing the combustion chamber from overheating. In summary, one has to reach a compromise while choosing different nozzle setups (HSI or LSI).

Although the previous results have confirmed the capability of the proposed burner concept in terms of efficient and stable burning of sulfur, they have been obtained for a fixed fuel to air

equivalence ratio at $\phi = 0.7$. In this case, the maximum flame temperature within the combustion chamber was above 2000 K, which is unfavorable with regard to the lifetime of the combustor and $NO_x$ formation. Therefore, it is imperative to extend the operating range to further fuel lean conditions to validate applicability of the sulfur burner. In particular, an attenuated flame stability is expected as a result of the reduced flame temperature and evaporation rate of sulfur, which may influence the overall operability of the burner. The objective of the current work is therefore to extend the obtained knowledge in ref 5 to fuel leaner conditions, which are more critical with regard to flame stabilization but beneficial in terms of burner operability at a lower flame temperature. A special focus is laid on a quantitative assessment of the $NO_x$ formation, which represents the main contamination from the sulfur combustion process.

The experimental investigation of sulfur combustion represents a challenging task, because sulfur is solid at atmospheric conditions and has to be liquefied before entering the burner system. In addition, the flue gas containing $SO_x$ has to be captured or recycled as a result of its toxicity and corrosiveness (by contact with water). Moreover, many relevant parameters, such as the flow or mixing fields, are not accessible by means of state of the art measurement techniques. Accordingly, numerical simulations have been conducted in this work, which provide fundamental knowledge for operating the burner in real scale conditions. To calculate the $NO_x$ output from the burner, new S/N/O and $NO_x$ reactions have been developed in addition to the base oxidation reactions, which are used for the simulations of sulfur combustion in this work.

The work is outlined as follows: The designed burner system for sulfur combustion and preliminary experimental results are first introduced. Thereafter, the development of reactions considering S/N/O interactions and $NO_x$ formation is described. The new reaction mechanism has been first applied to calculate zero dimensional (0D) batch reactors to study the ignition of sulfur at different operating conditions. Then, the numerical models and setups used for the three dimensional (3D) simulations of the real burner are presented, which are followed by an extensive discussion of the simulation results with respect to flame stabilization and $NO_x$ formation caused by different nozzle configurations. The work is summarized at the end.
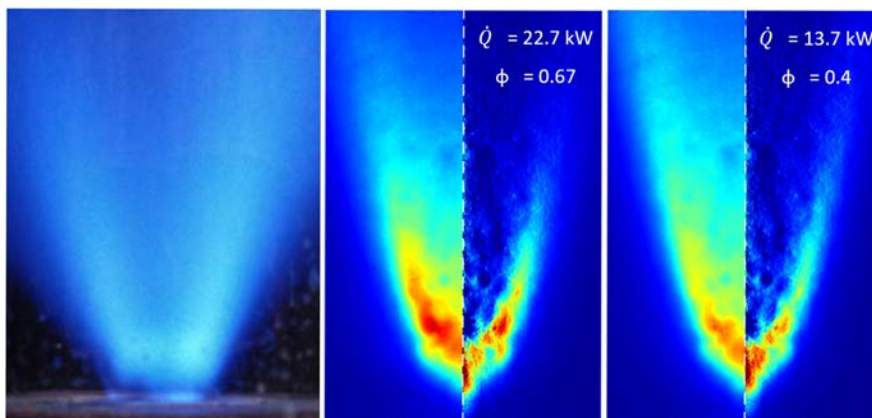
**Figure 3.** Flame structures of sulfur combustion from a laboratory scale, double concentric swirl burner at different equivalence ratios and under atmospheric pressure.

## BURNER DESIGN

**Main Components.** A laboratory scale burner for combustion of sulfur is designed and built, which is able to be operated with thermal loads of up to 50 kW, corresponding to a power density of more than 5 MW/m$^3$ at ambient pressure. Dependent upon the used swirl generators for the airflow and the operational equivalence ratio, the overall flame temperature is targeted to be below 1700 K, which ensures a long term stable operation of the burner and reduces NO$_x$ formation. The air inlet temperature of the combustor at its nominal condition is approximately 720−790 K, which corresponds to the air temperature after compression to 15 bar. Figure 2 shows a cross section view of the conceptual design of the double concentric swirl burner, which consists of the following main components: (1) Atomizer: molten sulfur is injected from a pressure swirl atomizer, which is located along the central axis of the burner and connected to the sulfur supply. The axial position of the atomizer can be adjusted through distance plates. The atomizer creates a hollow cone shaped spray downstream in the reaction zone. The design concept also allows for the application of an alternative sulfur supply from the side to operate in a pure airblast mode for future studies. (2) Swirler: two annular (a primary and a secondary) swirl generators are used to accomplish highly swirled airflows for an efficient evaporation and burning of sulfur spray from the atomizer. The primary airflow meets the spray issued from the pressure atomizer within the prefilmer. The secondary airflow bypasses the external channel confined by the prefilmer and the diffusor, which mixes with the sulfur spray and primary airflow at the orifice of the prefilmer. The design of the nozzle allows for modulation of the airflow swirl intensity by varying the blade angle of the swirlers. (3) Combustion chamber: combustion takes place downstream of the exit of the diffusor in a combustion chamber, which is made out of glass to ensure optical access to the flame. The chamber has a cylindrical shape with a diameter of 160 mm and a total length of 600 mm to ensure complete burnout of the sulfur spray.

In comparison to conventional burners operated with liquid fossil fuels, e.g., in aero engines or gas turbines, an additional sulfur supply system with a thermal conditioning system has to be included to feed molten sulfur above its melting point temperature. The combustion chamber is connected with a system for aftertreatment of exhaust gas, which collects the products from sulfur combustion (mainly SO$_2$ and SO$_3$) in an alkaline solution.

**Preliminary Experimental Results.** On the left of Figure 3 shows a snapshot of a sulfur flame from the proposed burner while using a LSI setup, which yields a blue luminescent color. On the right of Figure 3, chemiluminescence imaging of the sulfur/air flame is illustrated. There, the mass flow rate of air is kept constant, and that of sulfur decreases from left to right, which leads to a decrease of the overall equivalence ratio and thermal load. The left parts of these chemiluminescence images indicate line of sight integrated intensities,

and the right parts indicate the Abel transformed data for a cutting plane passing through the centerline axis. The flame yields a V shaped structure in all cases, which is attributed to the hollow cone spray generated by the pressure swirl atomizer. An additional contribution for spreading of the sulfur spray or the reaction zone is attributed to the swirled airflow. The opening angle of the V flame decreases slightly with decreased $\phi$, which can be explained by the decreased mass flow rate of sulfur from the pressure atomizer and the reduction of radial momentum of droplets. In this case, the pressure atomizer results in a smaller angle for the hollow cone spray. Another reason is the weakened effect of thermal expansion with decreased $\phi$ as a result of the combustion reaction, which results in a decreased radial flow velocity.

The preliminary experimental results shown in Figure 3 confirm the applicability of the proposed burner system for a moderate range of thermal loads, which is important considering a flexible load for future energy conversion systems. The test rig is in a commissioning phase to ensure a full insulation of the combustion chamber against the ambiance and to incorporate quantitative measurement techniques for the flame temperature and analyses of the exhaust gas. Therefore, the comparison of the simulation with the experiment cannot be the focus of the investigation at the current stage. Instead, the objective of the current work is to further assess the operational efficiency of the proposed burner at extremely fuel lean conditions, to achieve a lower flame temperature and NO$_x$ formation during the combustion of sulfur, which is, however, more challenging regarding evaporation and flame stabilization.

## NO$_X$ FORMATION DURING COMBUSTION OF SULFUR

**Development of Reactions for S/N/O Interactions.** One focus of this work is to quantitatively evaluate the NO$_x$ formation resulting from the sulfur combustion process. Therefore, the previously applied sulfur/oxygen reaction mechanism[9] has to be extended with reactions describing S/N/O interactions, in particular, the formation paths of NO$_x$ formed through sulfur oxidation. For this purpose, new reactions describing the S/N/O association have been investigated.

The thermodynamic properties of the species involved in the S/N/O system are first estimated with the help of computational chemistry (*ab initio* at different levels of calculation) using the Gaussian 16 program suite.[10,11] Structures and enthalpies of formation, entropies, and heat capacities for a series of stable molecules, radicals, as well as transition state structures, which estimate the energy barrier of a reaction, are calculated. The kinetic parameters for the plausible reactions describing this system are derived from the canonical transition state theory and using the quantum Rice−Ramsperger−Kassel (QRRK) analysis.[12] Detailed data of the above investigations are reported in a previous study.[13] A brief illustration of the calculation process is outlined in Figure 4, which illustrates the
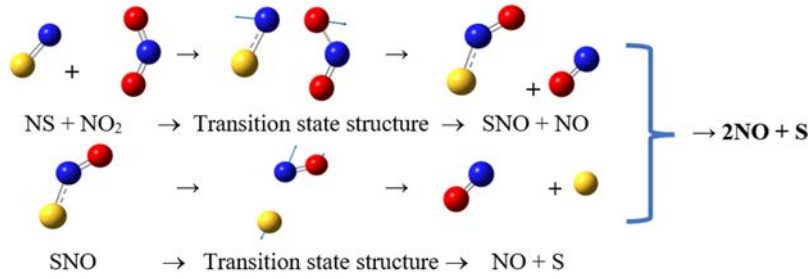
**Figure 4.** Illustration example for the development of a reaction concerning NO formation during sulfur combustion.
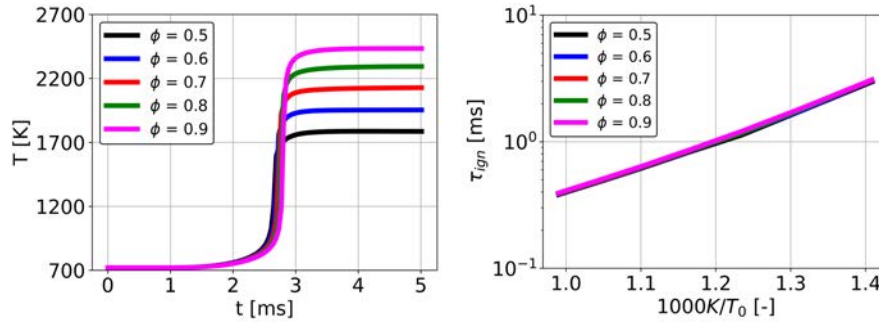


**Figure 5.** (Left) Time evolution of the flame temperature at different equivalence ratios and (right) dependency of ignition delay with the initial temperature calculated from simulations of 0D homogeneous reactors.
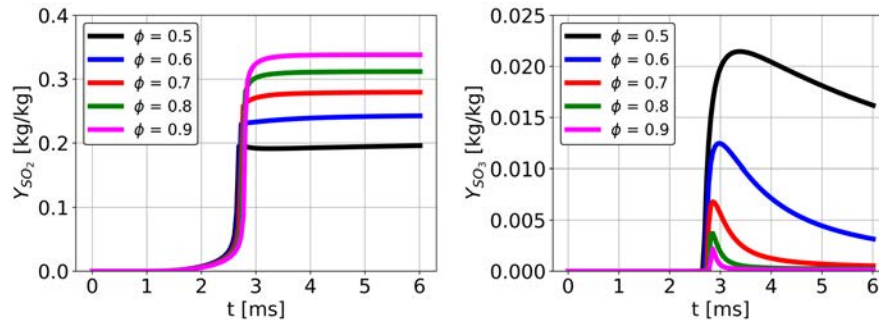


**Figure 6.** Temporal evolution of (left) $SO_2$ and (right) $SO_3$ calculated from 0D homogeneous reactor simulations.

reaction/association of $NO_2$ + NS to form SNO + NO. As seen in the figure, the nitrogen atom (blue) of SN approaches oxygen (red) of $NO_2$ to form an intermediate structure, a so called transition state structure, which undergoes the O−NO cleavage and results in a set of new products, SNO and NO. Formed SNO undergoes a S−NO bond scission to form NO and a S atom. The newly developed reaction mechanism for sulfur combustion, including $NO_x$ formation and S/N/O bonds, contains 19 species ($S_2$, S, SO, $SO_2$, $SO_3$, SSO, SN, SNO, $O_2$, O, N, $N_2$, NO, $NO_2$, $N_2O$, $NO_3$, $N_2O_4$, $N_2O_3$, and NNO) and 52 elementary reactions.

Unfortunately, no proper validation of the proposed mechanism could be performed because, as far as we are aware, very little experimental data involving the oxidation of pure sulfur (without hydrocarbons) are available. However, the accuracy of some of our thermochemical results could be compared and validated to the available literature studies, showing good agreement. These results are important because the kinetic parameters are mainly based on the accuracy of the thermochemical data, especially the determination of the transition state structures. The complete reaction mechanism used for the simulations of sulfur spray combustion is given in the Supporting Information.

**Computation of Sulfur Ignition and $NO_x$ Formation in 0D Homogeneous Reactors.** During the spray combustion process, sulfur droplets are injected into an environment with hot air, which then evaporate and mix with ambient air, forming an ignitable

mixture. There, the evaporation and mixing processes control the nature of the combustion, which are strongly dependent upon local temperature and flow conditions. In this case, combustion of the sulfur vapor/air mixture takes place under locally inhomogeneous, time varying equivalence ratios and preheating temperatures. Therefore, simulations of 0D homogeneous reactors have first been conducted in this section to study the behavior of sulfur combustion considering possible ignition conditions in the proposed sulfur burner. For this study, the equivalence ratio $\phi$ has been varied in the range of $0.5 \leq \phi \leq 0.9$ concerning the application cases, where the sulfur burner is operated under fuel lean conditions, and the initial temperature of the mixture starts at the designed intake airflow temperature at $T_0 = 720$ K.

On the left of Figure 5 depicts the temporal evolution of the flame temperature $T$ during the ignition process for different $\phi$. The initial conditions of the mixture are set to temperature $T_0 = 720$ K and pressure $p_0 = 1$ bar. After a slow increase of $T$ in an early stage in the range of $t < 2.5$ ms, $T$ increases drastically from around $t = 2.8$ ms until the close to equilibrium state at $t > 3$ ms. The adiabatic flame temperature $T_{ad}$ increases with $\phi$, which is largest for the near stoichiometric mixture ($\phi = 0.9$) with $T_{ad} \approx 2400$ K. For $\phi = 0.5$, which is used for the numerical simulations later, $T_{ad}$ reaches approximately 1800 K. The time point with a sudden increase of $T$ indicates the onset of ignition, which is noticed as the ignition delay $\tau_{ign}$ and shown on the right of Figure 5. The logarithm of $\tau_{ign}$ increases
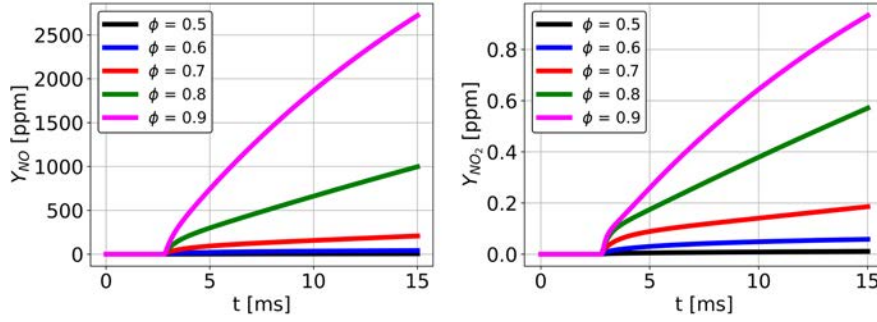
**Figure 7.** (Left) NO and (right) $NO_2$ formations during ignition of sulfur/air mixtures at different equivalence ratios.
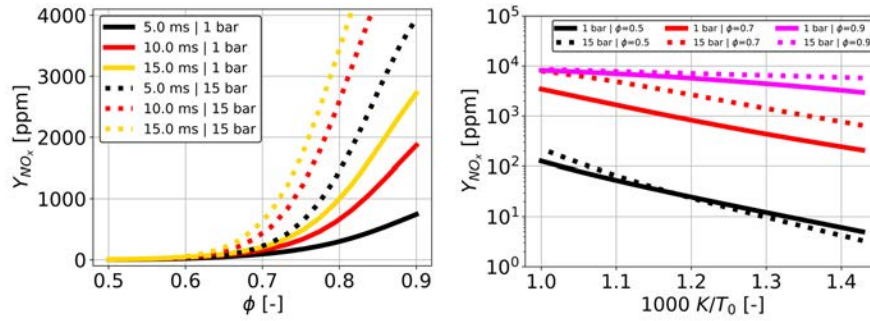


**Figure 8.** $NO_x$ formation from premixed sulfur/air combustion in dependence of (left) equivalence ratios and (right) preheating conditions.

quasi linearly with the inverse value of the start temperature $T_0$, which is almost independent of $\phi$. The same behavior was reported in the previous study,[9] where no S/N/O bonds were considered. Therefore, the newly included chemical species and elementary reactions with respect to S/N/O interactions have only a subordinate effect on the bulk heat release for sulfur combustion. This is reasonable as a result of the minor amount of the S/N/O species compared to the main species.

In Figure 6, the mass fractions of the main combustion products $SO_2$ (left) and $SO_3$ (right) are plotted against time. The mass fraction of $SO_2$ increases with $\phi$ and correlates strongly with those of the flame temperature (see on the left of Figure 5), indicating that the formation of $SO_2$ represents the main source of heat release during sulfur combustion. On the contrary, the mass fraction of $SO_3$, shown on the right of Figure 6, is considerably lower compared to that of $SO_2$, which decreases with $\phi$. This is attributed to the fact that the surplus of air at fuel lean conditions enhances oxidation of $SO_2$ to $SO_3$.

Figure 7 shows the time evolution of the mole fractions of NO (left) and $NO_2$ (right) during ignition of premixed sulfur/air mixtures at different $\phi$ for $p_0 = 1$ bar and $T_0 = 720$ K. In general, both NO and $NO_2$ increase with the residence time, and the mole fraction of NO is around 3 orders of magnitude larger than that of $NO_2$. In addition, the mole fractions of NO and $NO_2$ increase with $\phi$, which is in accordance with the dependency of the flame temperature upon $\phi$. Therefore, the increase of $NO_x$ formation with $\phi$ is attributed to the increased flame temperature with $\phi$.

On the left of Figure 8 shows the mole fraction of $NO_x$ (given by the sum of NO and $NO_2$) in dependence of $\phi$, which is evaluated for two different pressure conditions at $p_0 = 1$ and 15 bar. The condition of $p_0 = 15$ bar is taken in these plots, because the burner is planned to be operated at 15 bar for future real scale applications. For all considered residence times at $t = 5$, 10, and 20 ms, an increase of the $NO_x$ mole fraction with $\phi$ can be detected for different $p_0$, which is attributed to the increased flame temperature with $\phi$ (see Figure 5). An increase of the reactor pressure results in an increased $NO_x$ formation, particularly in the range of large $\phi$, with $0.7 < \phi < 0.9$. Therefore, it is preferred that the burner operates at the most possible lean conditions to reduce $NO_x$ formation.

On the right of Figure 8, the $NO_x$ mole fraction in logarithmic scale (evaluated for the residence time of 20 ms) shows a quasi linear decrease with the reciprocal value of $T_0$, again revealing that an increased flame temperature with $T_0$ will lead to an enhanced $NO_x$ formation. The quasi linear behavior of $\log(NO_x)$ with $1/T_0$ indicates that the formation of $NO_x$ is dominated by the temperature dependency of the reaction rate with respect to the reaction kinetic law, i.e., $\dot{r}_{NO_x} \propto \exp[-E_A/(RT)]$, with the activation energy $E_A$ and the universal gas constant $R$.

**Reaction Flux Analysis.** The net mass flux of nitrogen atoms during combustion of sulfur at $T_0 = 720$ K, $p_0 = 1$ bar, and $\phi = 0.5$ is illustrated in Figure 9 at a residence time of 20 ms. All fluxes are normalized with respect to the highest net flux between any two species. The arrows between the species show the net direction of the flux of nitrogen atoms. The first number shows the relative flux, which is split into the relative flux in forward and backward directions below. Only pathways with a total relative flux higher than $10^{-4}$ are presented in Figure 9. The reaction of $N_2$ starts with the oxidation with O, which produces a N atom and NO. Because of this, the highest flux of nitrogen atoms is between $N_2$ and N on the left of Figure 9 as well as $N_2$ and NO in the central pathway, which are both assigned a relative flux of 1. Starting from the black vertical arrow between $N_2$ and NO in the middle, which represents the reaction $N_2 + O \leftrightarrow N + NO$, a forward flux of 1.0 and a backward flux of approximately 0.0008 result in a total relative flux of 1 toward NO. For the investigated time instant, NO is formed mostly from this reaction and the reaction $N + O_2 \leftrightarrow NO + O$ (left path in Figure 9). These reactions are also available in the Zeldovich mechanism commonly used for computations of thermal $NO_x$ formation from combustion of fossil fuels.[14] A small share of $NO_2$ is formed in reactions $NO + O + M \leftrightarrow NO_2 + M$ and $NO + O_2 \leftrightarrow NO_2 + O$. In these reactions, a large relative flux of nitrogen can be observed in the forward and backward directions ($\approx$1.6). However, because the fluxes in both directions are almost equal, the resulting total relative flux is small ($\approx$0.004). The relative nitrogen fluxes toward NO with a value of 1 and toward $NO_2$ with a value of ca. 0.002 are in agreement with the results presented in Figure 7, where the mole fraction of NO is approximately 3 orders of magnitude higher than that of $NO_2$.
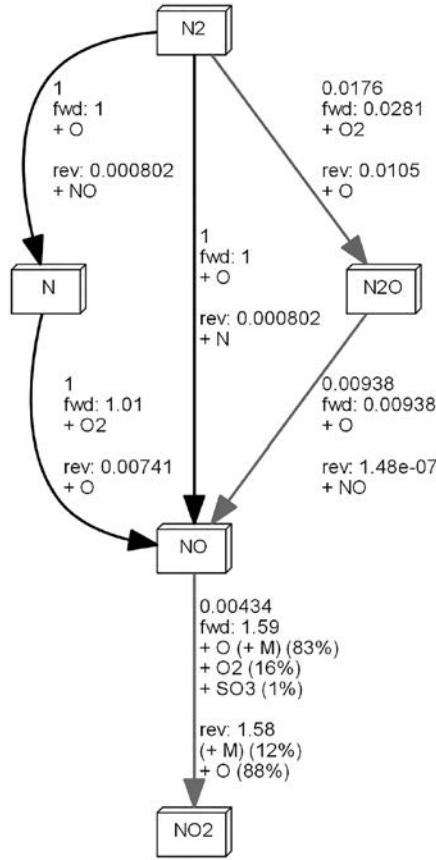
**Figure 9.** Chemical pathways illustrating the formation of $NO_x$ from the nitrogen atom during sulfur/air combustion at the conditions of $T_0 = 720$ K, $p_0 = 1$ bar, $\phi = 0.5$, and a residence time of 20 ms.

## SIMULATION METHODS

**Multiphase Flow.** Because a complete simulation of the multiphase flow, including both the primary and secondary atomization, is computationally too expensive, a hybrid Eulerian−Lagrangian method is used in this work to simulate the combustion process of liquefied sulfur. In this method, a large number of Lagrangian parcels, which represent collections of single spherical droplets with predefined velocities and size distributions, is injected from given inlets into the computational domain. These parcels are then tracked during the simulations with regard to their kinematic movements, heat and mass transfer with the surrounding gas flow. Two sets of balance equations are solved in this case: one for the dispersed phase with Lagrangian parcels and the other for the continuous Eulerian phase with the gas flow. Both sets of equations are coupled through their source terms in the conservation equations, which take multiphase heat and mass exchanges into account. The method has already been widely used to simulate spray combustion processes,[15−20] and a detailed description of the solved equations can be found in ref 5.

**Turbulence Modeling.** The large eddy simulation (LES) technique[21] has been used for modeling the turbulent flow in the Eulerian phase, which solves the spatially filtered set of the governing equations. The influence of small scale, unresolved flow structures has been modeled by means of a sub grid scale (SGS) model. Because the LES approach directly resolves the transient turbulent fluctuations down to the cutoff scale, it is well suited for studying overall flame dynamics and flame stabilization phenomena dominated by large scale flow structures. The algebraic Smagorinsky SGS model has been used in this work to render the unresolved Reynolds stresses. The SGS scalar transport is considered by a gradient transport approach assuming unity of Schmidt and Prandtl numbers.

**Combustion Modeling.** A finite rate chemistry model has been applied to evaluate the reaction rate in the gaseous phase, where a complex reaction mechanism for sulfur/air combustion considering $NO_x$ formation is used. The effect of turbulence on the mean reaction rate (turbulence−chemistry interaction) is modeled with the partially stirred reactor (PaSR) model,[22,23] which calculates the filtered reaction rate $\bar{\dot{r}}_k$ by a weighted average with the local chemical and turbulent time scales $\tau_{chem}$ and $\tau_{mix}$.

$$\bar{\dot{r}}_k = \frac{\tau_{chem}}{\tau_{chem} + \tau_{mix}} \dot{r}_k \tag{1}$$

The laminar reaction rate $\dot{r}_k$ of the $k$th species is calculated from the chemical kinetic rate law through the Arrhenius equation. $\tau_{chem}$ and $\tau_{mix}$ are computed from the laminar reaction rate and SGS turbulence modeling.

**Submodels.** In addition to these basic modeling concepts, a number of submodels have been used to consider additional physical phenomena related to the dispersed phase: (1) Reitz Diwaka's breakup model,[24] where initial droplets can further break down into smaller droplets based on the local droplet Weber number $We$; (2) O'Rourke model,[25,26] in which a probability of collision of all possible pairs of parcels is calculated and two possible modes of collision are assumed, i.e., coalescence and grazing; and (3) rebound model,[27] where the particles are bounced back after collision with a wall, neglecting loss of kinetic energy.

Because the same simulation methods are used as in our previous work,[5] a more detailed description of the solved equations and the connected submodels is omitted here.

## SIMULATION SETUPS

**Operating Conditions.** Table 1 lists the operating parameters used for the 3D simulations of sulfur combustion. The laboratory

**Table 1. Operating Parameters Used for the Simulations of Sulfur Combustion**

| $p_0$ (bar) | $T_{air}$ (K) | $T_{sulfur}$ (K) | $\dot{m}_{air}$ (kg/h) | $\dot{m}_{sulfur}$ (kg/h) | $u_{bulk}$ (m/s) | $Re$ | $\dot{Q}$ (kW) |
|---|---|---|---|---|---|---|---|
| 1 | 720 | 420 | 43.8 | 5.21 | 30.1 | 14,150 | 14 |

scale burner is operated at atmospheric conditions with $p_0 = 1$ bar. The mass flow rates $\dot{m}$ for the sulfur and air flows shown in Table 1 lead to an equivalence ratio of $\phi = 0.5$. The thermal load of the burner is $\dot{Q} \approx 14$ kW, with the heating value of sulfur given by $H_S = 9.6$ MJ/kg. $u_{bulk}$ and $Re$ are the bulk flow velocity and airflow Reynolds number calculated at the exit plane of the nozzle. Two sets of the swirl generators have been studied in this work, which cause low and high swirl intensities (LSI and HSI). The theoretical swirl numbers for the primary and secondary swirlers are 0.46 and 0.81 in the HSI case and 0.76 and 0 in the LSI case.

**Computational Grid.** To reproduce the complex internal flow field within the nozzle, the computational domain is constructed to include all major components of the nozzle (see Figure 2, too), i.e., the pressure atomizer located along the centerline axis, two annularly oriented radial swirl generators, the prefilmer, and the diffusor, as shown in Figure 10. Preheated air enters the domain from the annular boundary on the left, which is redirected to pass through the primary and secondary swirlers. The combustion chamber is treated as an adiabatic, no slip wall. At the outlet boundary, gradients of all transport variables are set to zero and the total pressure is set to 1 bar. The computational grid consists of approximately 1 million cells, with an equidistant grid size of 1.9 mm (cubic root of cell volume) for resolving the nozzle internal flow field and the flame stabilization zones.

**Injection Model.** Sulfur spray is injected from an annular disk with an inner diameter of 15 mm and an outer diameter of 16 mm, which is located 9 mm upstream of the nozzle exit using a presumed size distribution. The Rosin−Rammler distribution is used to describe the probability density function of the size of the injected droplets.
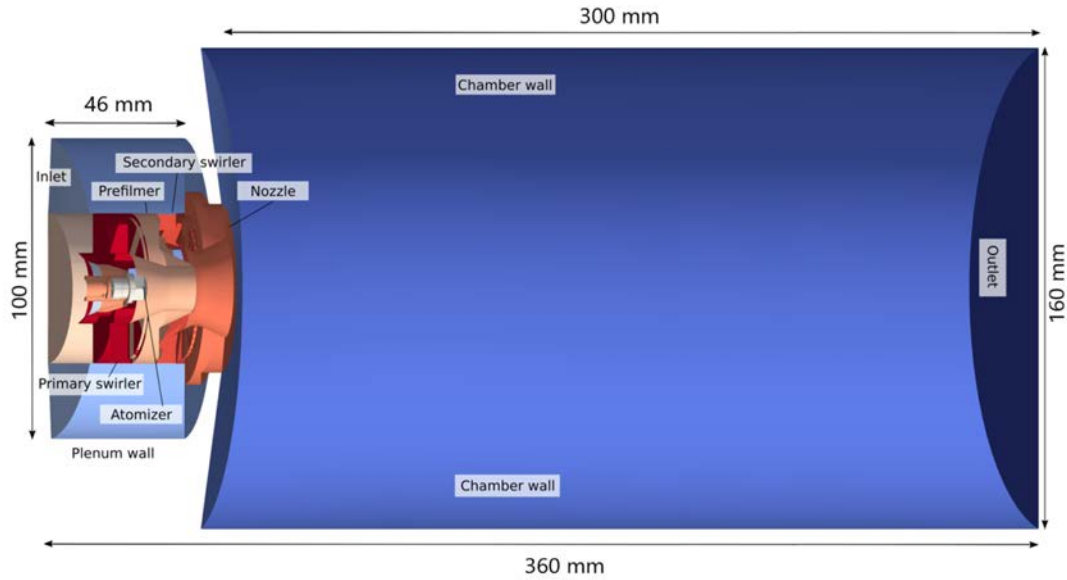
**Figure 10.** Cut view of the computational domain, along with indications of boundary conditions.

The parameters for the Rosin−Rammler function are set according to results of previous PDA spray experiments for the same burner shown in ref 4, which yields a Sauter mean diameter (SMD) of 41 $\mu$m. Figure 11 compares the presumed droplet size distribution with the
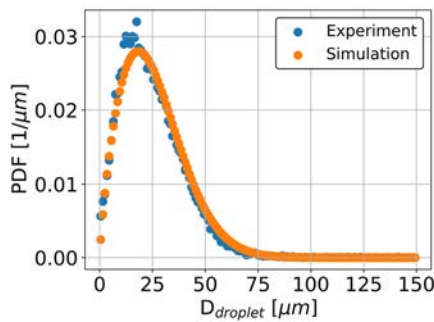


**Figure 11.** Comparison of the measured droplet size distribution with a modeled Rosin−Rammler distribution used for the simulation.

measured droplet size distribution, which shows good agreement. The number of injected parcels (collections of sulfur droplets) per second is set to 4.5 million, which represents a compromise between simulation accuracy and computational effort.

**Numerical Setups.** The simulations have been performed using the open source CFD code OpenFOAM, version 2006, which solves the governing equations for the continuous phase by means of the finite volume method. A fully implicit compressible formulation of the set of equations is used, along with the central difference scheme (second order, unbounded) for discretization of the convective and diffusion terms. The pressure implicit split operator (PISO) algorithm has been used for pressure correction. The simulations have been performed with the standard solver sprayFoam available in Open FOAM, which uses the aforementioned hybrid Eulerian−Lagrangian approach. The required material properties of gaseous and liquid sulfur, such as the density, the viscosity, the vapor pressure, and the vapor temperature, have been implemented into the OpenFOAM code.

## RESULTS

**Spray Characteristics.** Spray dispersion plays an essential role for the evaporation, mixing, and combustion processes, which determine the location of the reaction zones. Figure 12
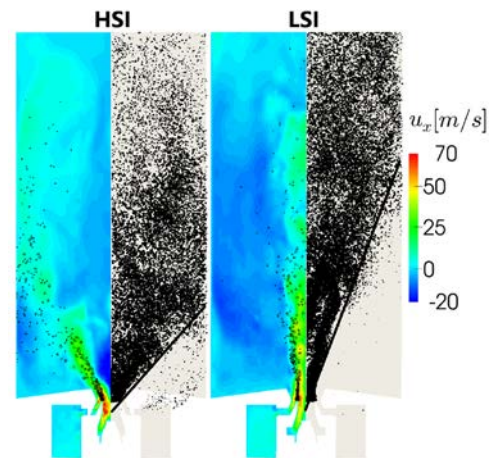


**Figure 12.** Spray dispersion on a cutting plane passing through the centerline axis and side view caused by the (left) HSI and (right) LSI nozzles.

shows snapshots of calculated spatial distributions of droplets for different nozzle setups with a HSI and LSI. The left part of each subplot represents a meridian view through the centerline axis colored by contours of the streamwise velocity $u_x$, and the right part represents the line of side view of the full 3D spray. The diameter of the droplets is scaled by a factor of 20 for better visualization. The HSI nozzle results in a strong IRZ, which can be detected from the contours of flow velocity for the HSI case in Figure 12. The IRZ leads to a broader spray and longer residence time for the droplets compared to the LSI nozzle, so that most of the introduced sulfur droplets can be evaporated. However, the IRZ in the HSI case leads to a large number of sulfur droplets hitting the chamber wall. The opposite effect is found for the LSI burner, with less droplets hitting the wall but an extended spray in the streamwise direction with more droplets leaving the computational domain. This is attributed to the higher axial momentum caused by the lower swirl intensity, which can be detected in Figure 12 by the contour plot of $u_x$ for the LSI case.

Table 2 summarizes the resulting spray angles as well as the quantitative shares of droplets hitting the chamber wall and

**Table 2. Comparison of Calculated Spray Properties Using the HSI and LSI Nozzles**

| burner setup | spray angle (deg) | droplet wall collisions (%) | escaped droplets (%) |
|---|---|---|---|
| HSI | 40 | 4.05 | 0.15 |
| LSI | 17 | 1.65 | 4.14 |

those escaping the simulation domain caused by the HSI and LSI nozzle setups. Collision of sulfur droplets with the wall should be avoided as much as possible to save long term operation of the burner. On the other hand, the overall evaporation efficiency can be evaluated from the difference of injected and escaped fuel droplets in Table 2. Therefore, the escaped liquid sulfur mass should be kept as small as possible for a high burning efficiency. As a consequence, one has to make a compromise while choosing HSI or LSI configurations in terms of operability and combustion efficiency.

The result with respect to comparison of the HSI and LSI nozzles is qualitatively similar to those obtained in our previous work,[5] where $\phi = 0.7$ was used. However, the penetration range of the spray and the shares of droplets hitting the chamber wall and escaping the domain are considerably increased under the current fuel leaner conditions, which are attributed to the lowered overall flame temperature as well as the resulting decrease of the evaporation rate. It is therefore of particular importance to extend the previously obtained knowledge to further fuel lean conditions, which constitutes the objective of the current work.

**Flame Stabilization.** Figure 13 shows instantaneous (left part of each plot) and time mean (right part of each plot) contours of the flame temperature $T$ (top) and heat release rate $\dot{q}$ (bottom) from simulations of the burners with a HSI (left) and a LSI (right) nozzle. The V shaped reaction zones can be identified from the contours of $\dot{q}$, which are shorter and
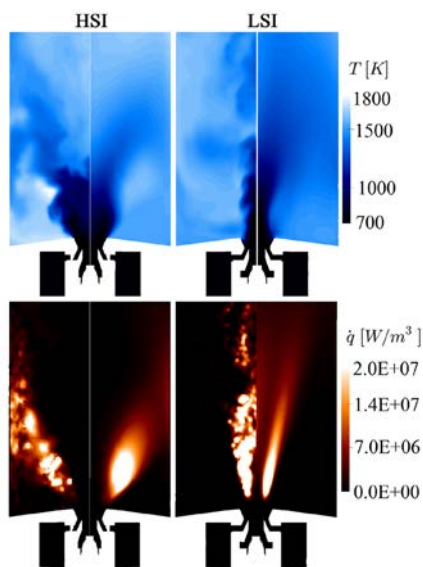


**Figure 13.** Instantaneous and time mean contours of (top) temperature and (bottom) heat release rate calculated from simulations of sulfur combustion using the (left) HSI and (right) LSI burner.

broader for HSI compared to the LSI nozzle. This difference is attributed to the IRZ caused by the highly swirled flow in the HSI case. In contrast, the fuel droplets in the LSI case yield high momentum in the streamwise direction, which results in a stronger penetration of the spray and the reaction zone extending further downstream. The overall flame temperature is higher for HSI compared to the LSI nozzle as a result of the reinforced evaporation and mixing caused by the IRZ in the HSI case. This leads to a locally increased equivalence ratio. The total heat release rates evaluated from volume integration of the local heat release rate are approximately 16 kW for both the HSI and LSI cases, which correspond to a power density of approximately 2.6 MW/m$^3$.

In Figure 14, the flame shape and the lift off height evaluated from the simulation in terms of time mean $\dot{q}$ (left) and the chemiluminescence measurement (right) show a reasonable agreement for the LSI nozzle configuration. Although the overall equivalence ratio is kept constant at $\phi = 0.5$, the mass flow rate used for the experiment is larger compared to that used in the simulation. As a result, the flame obtained from the experiment is slightly broader compared to that from the simulation. In addition, the measured chemiluminescence intensity at the base of the flame is large near the centerline axis, whereas $\dot{q}$ from the simulation is almost zero there. This could be attributed to Abel transformation of the light intensity data from 3D volume data to a two dimensional (2D) slice. Note that even the measurements on the lab scale sulfur burner represent an extremely challenging task as a result of the underlying complex chemophysical processes (phase change from solid to liquid to gas, atomization, spray formation, evaporation, mixing, combustion, toxicity of the reaction product, etc.). Therefore, a quantitative assessment directly within the sulfur spray flame is not feasible.

Figure 15 displays the correlations of time mean flame temperature $T$ against the local equivalence ratio $\phi_{loc}$, which is evaluated by the ratio of the available mass fraction of sulfur from all chemical species to the stoichiometric mass fraction of sulfur in all grid cells. $\phi_{loc}$ spans over a wide range from 0 to ca. 0.8, although the overall equivalence ratio is set to $\phi = 0.5$. In Figure 15, $T$ increases almost linearly with $\phi_{loc}$, which is in accordance with the calculated flame temperature in depend ence of $\phi$ obtained from simulations of 0D homogeneous reactors (see on the right of Figure 5). The HSI nozzle results in a higher maximum $\phi_{loc}$ and $T$ compared to the LSI nozzle, which is due to the reinforced evaporation and mixing processes sustained by the strongly swirled airflow. The dotted line in Figure 15 represents solutions from calculations of the 0D homogeneous reactors for different $\phi$ at 1 bar and 720 K, which yields a quasi linear correlation for the equilibrium flame temperature against $\phi$, too. The flame temperatures from the 3D simulations are however lower than those obtained from the 0D solutions. The reason is attributed to evaporation of the sulfur spray, which results in a lower mixture temperature (compared to the air temperature at 720 K) for ignition of the sulfur/air mixture, because the energy consumed by phase change of sulfur is not considered in the 0D calculations.

Although the overall flame structures given by the V shaped flames are similar to those shown in ref 5, the flames are lifted slightly from the nozzle for both HSI and LSI nozzles as a result of the very lean condition used in this work (see contours of the heat release rate at the bottom of Figure 13). Furthermore, the overall flame temperature is lower compared to the previous simulations shown in ref 5, which leads to a
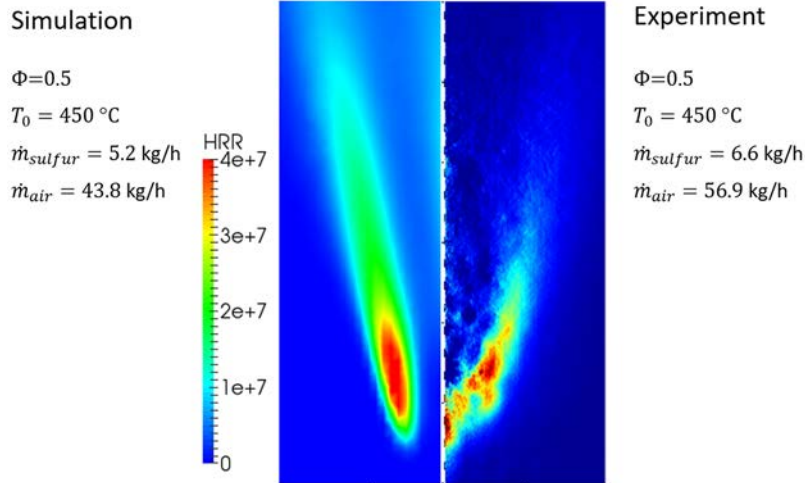
**Figure 14.** Comparison of the calculated heat release rate to the chemiluminescence measurement for the LSI setup on a cutting plane passing through the centerline axis.
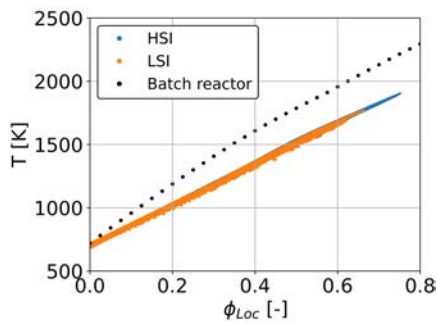


**Figure 15.** Correlations between time mean temperature and equivalence ratio for the HSI and LSI nozzles.

slower evaporation of the droplets and elongated flames directed downstream. As shown in Figure 12, a large number of droplets collide against the side wall of the combustion chamber in the HSI case, so that chemical reactions take place, even in direct vicinity of the wall (see the lower left plot in Figure 13). The results reveal an increased risk regarding flame stabilization and lifetime of the burner while operating the combustor under the current fuel lean conditions.

**NO$_x$ Formation.** Because the combustion products SO$_x$ are recaptured and reused in the solar−sulfur cycle, NO$_x$ remains the major contaminant, which has to be minimized or segregated from the combustion product. In the previous work,[5] the simulations were focused solely on evaluating the overall burner design concept; therefore, NO$_x$ formation has not been considered. In the current work, NO$_x$ formation reactions as well as newly developed chemical reactions considering S/N/O interactions have been included. Figure 16 compares time averaged mole fractions of NO (left) and NO$_2$ (right) caused by the HSI and LSI burners. The mole fraction of NO is larger by approximately orders of magnitude than that of NO$_2$. The same behavior has been shown for the calculations of the 0D homogeneous reactor, as shown in Figure 7. Therefore, NO represents the main contributor in terms of NO$_x$ formation. In addition, the share of NO correlates strongly with the temperature distributions (see Figure 13 at the top), which can be explained by means of the reaction flux analysis from the 0D autoignition calculations shown in Figure 9. There, the largest share of the nitrogen flux
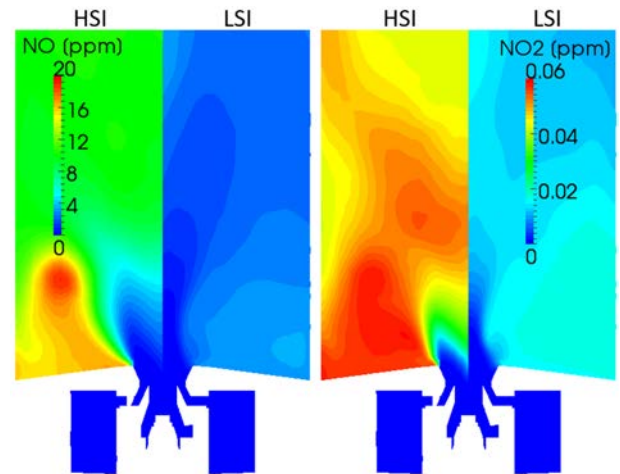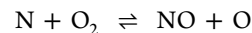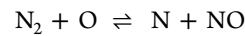


**Figure 16.** Time averaged contours of (left) NO and (right) NO$_2$ mole fractions from simulations of sulfur combustion using the HSI and LSI nozzles.

has been confirmed to be attributed to the Zeldovich mechanism through the following reactions:

$$N_2 + O \rightleftharpoons N + NO$$

$$N + O_2 \rightleftharpoons NO + O$$

These reactions are mainly controlled by the temperature and become relevant particularly in the high temperature range. Therefore, the HSI nozzle yields a higher NO or NO$_x$ formation compared to the LSI nozzle as a result of the higher flame temperature, as shown in Figures 13 and 15.

The correlation between the flame temperature and NO$_x$ formation is further elucidated in Figure 17. The diagram has been made by conditional averaging of all data pairs with the time mean NO$_x$ mole fraction and flame temperature from each cell volume using a bin width of 10 K. For both HSI and LSI nozzles, the share of NO$_x$ increases first slowly with the flame temperature until a threshold point of $T \approx 1600$ K; NO$_x$ is then formed drastically with the temperature further increased. The behavior coincides with the threshold point, above which the Zeldovich mechanism responsible for NO$_x$ formation becomes dominant. In the whole temperature range,
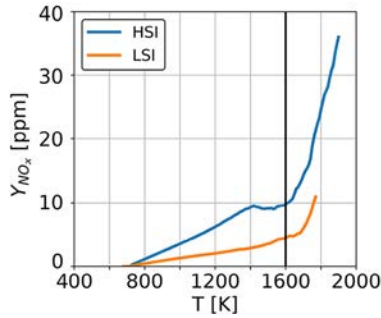
**Figure 17.** Comparison of the correlations of local mole fractions of $NO_x$ to the temperature from the HSI and LSI nozzles.

the $NO_x$ concentration is larger in HSI compared to that from the LSI case, which is attributable to the longer residence time provided by the strong recirculating flow by the HSI configuration. Because the flame reaches a higher maximum temperature in HSI compared to the LSI case (see Figure 15), the peak value of $NO_x$ from the HSI is considerably higher than that formed by the LSI burner.

The same behavior can be detected in Figure 18, which shows the mass flow rates of $NO_x$ plotted against the
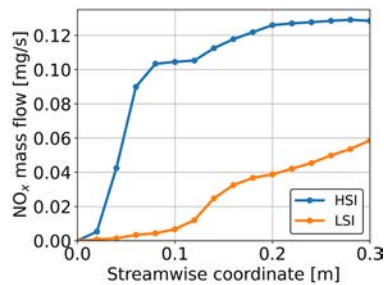


**Figure 18.** Comparison of the $NO_x$ mass flow rate along the streamwise coordinate from HSI and LSI nozzles.

streamwise coordinate. The location with the streamwise coordinate at 0 indicates the exit plane of the nozzle. The mass flow rate from the HSI nozzle is characterized by a rapid growth close to the nozzle, which is followed by a slower increase downstream. The LSI setup, however, yields a moderate increase for the $NO_x$ mass flow along the streamwise axis. This difference can be explained by the associated flame shapes with the HSI and LSI nozzles, as shown in Figure 13. There, the HSI flame yields a broader and shorter reaction zone compared to the LSI flame. As a consequence, the flame temperature and amount of $NO_x$ increase faster along the streamwise axis in HSI compared to the LSI burner.

The first two columns in Table 3 list calculated $NO_x$ mass and mole fractions averaged over the exit plane, indicating that the predicted $NO_x$ formation from the HSI nozzle is more than 2 times higher than that from the LSI nozzle. The third column in Table 3 reveals the generated $NO_x$ mass per kWh, which is evaluated from the ratio of the $NO_x$ mass flow at the exit plane

**Table 3. Predicted $NO_x$ Emissions at the Outlet Plane of the Simulation Domain for HSI and LSI Burner Designs**

| $NO_x$ | (kg/kg) | (ppm) | (g/kWh) | $(mg/m_N^3)$ |
|---|---|---|---|---|
| HSI | $9.86 \times 10^{-6}$ | 10.7 | $2.94 \times 10^{-2}2$ | 14.2 |
| LSI | $4.34 \times 10^{-6}$ | 4.7 | $1.30 \times 10^{-2}$ | 6.0 |

and the total heat release rate. The volume specific $NO_x$ emissions calculated from the ratio of $NO_x$ mass flow rates and total volume flow rates at the outlet (converted to normal conditions) are given in the last column of Table 3, which reveal the expected amount of $NO_x$ while operating the sulfur burner. Note that operating the burner at elevated pressures will lead to an increased $NO_x$ formation, as shown in Figure 8 for the 0D homogeneous reactor.

## CONCLUSION

High fidelity numerical simulations of a newly developed double concentric swirl burner for combustion of sulfur have been conducted. The objective of the current work is to extend the knowledge regarding flame stabilization obtained from our previous work for further fuel lean conditions and to quantitatively evaluate the $NO_x$ formation from the sulfur combustion process. The simulations reveal a V shaped flame structure, which is stabilized by the swirled flow and shows a reasonably good agreement with preliminary experiments. In comparison to our previous simulations using a higher equivalence ratio, a strongly increased share of sulfur droplets colliding with the side wall and escaping the domain have been noticed in the current work. The reason has been shown to be attributed to the decreased flame temperature while burning under leaner conditions, which results in a weakened evaporation. In addition, the flames are lifted from the nozzle while operating the burner at the present lean conditions. Moreover, combustion reactions occur even very close to the chamber wall when using a highly swirled airflow.

The calculated $NO_x$ concentration increases almost linearly with the local flame temperature, and a drastic increase of $NO_x$ is detected when the local flame temperature is higher than 1600 K. The nozzle setup with a HSI yields a larger flame temperature compared to the nozzle configuration with a LSI, which is caused by a strong inner recirculation flow generated in the HSI case. Accordingly, the $NO_x$ formation from the HSI burner is more than 2 times higher than that from the LSI design. In summary, the LSI burner setup and an equivalence ratio as lean as possible are preferred with respect to $NO_x$ formation. However, these conditions are more prone to flame stabilization problems (lift off) and slower droplet evaporation (combustion efficiency). The results serve as essential knowledge for operating the proposed burner for sulfur combustion with a high power density.

## AUTHOR INFORMATION

### Corresponding Author

**Feichi Zhang** − *Engler Bunte Institute, Division of Combustion Technology, Karlsruhe Institute of Technology, Karlsruhe 76131, Germany;* orcid.org/0000 0003 3260 5808; Email: feichi.zhang@kit.edu

## Authors

**Maksymilian Kurjata** − *Engler Bunte Institute, Division of Combustion Technology, Karlsruhe Institute of Technology, Karlsruhe 76131, Germany*

**Nadia Sebbar** − *Engler Bunte Institute, Division of Combustion Technology, Karlsruhe Institute of Technology, Karlsruhe 76131, Germany;* orcid.org/0000 0001 9832 2398

**Thorsten Zirwes** − *Engler Bunte Institute, Division of Combustion Technology, Karlsruhe Institute of Technology, Karlsruhe 76131, Germany; Steinbuch Centre for Computing, Karlsruhe Institute of Technology, Karlsruhe 76131, Germany*

**Michal Fedoryk** − *Engler Bunte Institute, Division of Combustion Technology, Karlsruhe Institute of Technology, Karlsruhe 76131, Germany*

**Stefan Harth** − *Engler Bunte Institute, Division of Combustion Technology, Karlsruhe Institute of Technology, Karlsruhe 76131, Germany*

**Robert Wang** − *Engler Bunte Institute, Division of Combustion Technology, Karlsruhe Institute of Technology, Karlsruhe 76131, Germany*

**Peter Habisreuther** − *Engler Bunte Institute, Division of Combustion Technology, Karlsruhe Institute of Technology, Karlsruhe 76131, Germany*

**Dimosthenis Trimis** − *Engler Bunte Institute, Division of Combustion Technology, Karlsruhe Institute of Technology, Karlsruhe 76131, Germany*

**Henning Bockhorn** − *Engler Bunte Institute, Division of Combustion Technology, Karlsruhe Institute of Technology, Karlsruhe 76131, Germany*

## NOMENCLATURE

### Greek Symbols

$\phi$ = fuel equivalence ratio
$\phi_{loc}$ = local equivalence ratio
$\tau_{chem}$ = chemical time scale (s)
$\tau_{mix}$ = mixing time scale (s)
$\tau_{ign}$ = ignition delay time (s)

### Latin Symbols

$D$ = diameter (m)
$H_S$ = heating value of sulfur (MJ/kg)
$\dot{m}$ = mass flow rate (kg/h)
$p$ = pressure (Pa)
$\dot{q}$ = heat release rate (W/m$^3$)
$Q$ = thermal load (kW)
$\dot{r}$ = reaction rate (kg m$^{-3}$ s$^{-1}$)
$T$ = temperature (K)
$u$ = velocity (m/s)
$Y$ = mole fraction

### Dimensionless Numbers

$Pr$ = Prandtl number
$Re$ = Reynolds number
$Sc$ = Schmidt number
$We$ = Weber number

### Acronyms

CSP = concentrated solar power
HSI = high swirl intensity
IRZ = inner recirculation zone
LES = large eddy simulation
LSI = low swirl intensity
PaSR = partially stirred reactor
PDA = phase Doppler anemometry
SGS = sub grid scale
SMD = Sauter mean diameter

## REFERENCES

(1) Giaconia, A.; Iaquaniello, G.; Metwally, A. A.; Caputo, G.; Balog, I. Experimental demonstration and analysis of a CSP plant with molten salt heat transfer fluid in parabolic troughs. *Sol Energy* **2020**, *211*, 622−632.

(2) Agrafiotis, C.; Thomey, D.; de Oliveira, L.; Ebert, M.; Gobereit, B.; Pernpeintner, J.; Schlögl Knothe, B.; Alkan, G.; Roeb, M.; Sattler, C. A particle receiver driven thermochemical cycle employing elemental sulphur for solar thermochemical energy storage: Investigation of particles as concentrated sunlight harvesting media and sulphur trioxide splitting catalysts. *Sol Energy* **2022**, *234*, 21−38.

(3) German Aerospace Center (DLR). *PEGASUS (Renewable Power Generation by Solar Particle Receiver Driven Sulphur Storage Cycle)*; DLR: Jülich, Germany, 2021; https://www.pegasus project.eu (accessed Oct 17, 2021).

(4) Fedoryk, M.; Zhang, F.; Heidarifatasmi, H.; Sebbar, N.; Harth, S.; Trimis, D.; Bockhorn, H. Experimental and numerical inves tigations of a high power density sulphur burner. *Proceedings of the 12th European Conference on Industrial Furnaces and Boilers*; Porto, Portugal, April 14−17, 2020.

(5) Zhang, F.; Heidarifatasmi, H.; Harth, S.; Zirwes, T.; Wang, R.; Fedoryk, M.; Sebbar, N.; Habisreuther, P.; Trimis, D.; Bockhorn, H. Numerical evaluation of a novel double concentric swirl burner for sulfur combustion. *Renewable Sustainable Energy Rev.* **2020**, *133*, 110257.

(6) Agrafiotis, C.; Thomey, D.; de Oliveira, L.; Overbeck, N.; Thanda, V.; Roeb, M.; Sattler, C. Solar energy conversion and storage through sulphur based thermochemical cycles implemented on centrifugal particle receivers. *AIP Conf. Proc.* **2020**, *2303*, 170001.

(7) Zhang, F.; Heidarafitasmi, H.; Harth, S.; Zirwes, T.; Sebbar, N.; Fedoryk, M.; Trimis, D. Numerische Untersuchung eines Schwe felverbrennungssystems. *Proceedings of the 29th Deutscher Flammentag*; Ruhr Universität Bochum, Bochum, Germany, Sept 17−18, 2019.

(8) Zhang, F.; Heidarafitasmi, H.; Zirwes, T.; Fedoryk, M.; Harth, S.; Sebbar, N.; Habisreuther, P.; Trimis, D.; Bockhorn, H. Numerical simulation of sulfur combustors with high power density. *Proceedings of the 9th European Combustion Meeting*; Lisbon, Portugal, April 14−17, 2019.

(9) Sebbar, N.; Zirwes, T.; Habisreuther, P.; Bozzelli, J.; Bockhorn, H.; Trimis, D. S2 + Air Combustion: Reaction Kinetics, Flame Structure and Laminar Flame Behavior. *Energy Fuels* **2018**, *32*, 10184−10193.

(10) Frisch, M. J.; Trucks, G. W.; Schlegel, H. B.; Scuseria, G. E.; Robb, M. A.; Cheeseman, J. R.; Scalmani, G.; Barone, V.; Petersson,

G. A.; Nakatsuji, H.; Li, X.; Caricato, M.; Marenich, A.; Bloino, J.; Janesko, B. G.; Gomperts, R.; Mennucci, B.; Hratchian, H. P.; Ortiz, J. V.; Izmaylov, A. F.; Sonnenberg, J. L.; Williams Young, D.; Ding, F.; Lipparini, F.; Egidi, F.; Goings, J.; Peng, B.; Petrone, A.; Henderson, T.; Ranasinghe, D.; Zakrzewski, V. G.; Gao, J.; Rega, N.; Zheng, G.; Liang, W.; Hada, M.; Ehara, M.; Toyota, K.; Fukuda, R.; Hasegawa, J.; Ishida, M.; Nakajima, T.; Honda, Y.; Kitao, O.; Nakai, H.; Vreven, T.; Throssell, K.; Montgomery, J. A., Jr.; Peralta, J. E.; Ogliaro, F.; Bearpark, M.; Heyd, J. J.; Brothers, E.; Kudin, K. N.; Staroverov, V. N.; Keith, T.; Kobayashi, R.; Normand, J.; Raghavachari, K.; Rendell, A.; Burant, J. C.; Iyengar, S. S.; Tomasi, J.; Cossi, M.; Millam, J. M.; Klene, M.; Adamo, C.; Cammi, R.; Ochterski, J. W.; Martin, R. L.; Morokuma, K.; Farkas, Ö.; Foresman, J. B.; Fox, D. J. *Gaussian 16, Revision B.01*; Gaussian, Inc.: Wallingford, CT, 2016.

(11) Gaussian, Inc. *Gaussian*; Gaussian, Inc.: Wallingford, CT, 2021; https://gaussian.com (accessed Oct 17, 2021).

(12) Sheng, C.; Bozzelli, J.; Dean, A.; Chang, A. Detailed Kinetics and Thermochemistry of $C_2H_5$ + $O_2$: Reaction Kinetics of the Chemically Activated and Stabilized $CH_3CH_2OO^\bullet$ Adduct. *J. Phys. Chem. A* **2002**, *106*, 7276−7293.

(13) Sebbar, N.; Bozzelli, J.; Bockhorn, H.; Trimis, D. A Thermochemical Study of Reactions Occuring in the S−N−O System. *Proceeding of the 11th Mediterranean Combustion Symposium*; Tenerife, Spain, June 16−20, 2019.

(14) Joos, F. *Technische Verbrennung: Verbrennungstechnik, Ver brennungsmodellierung, Emissionen*; Springer: Berlin, Germany, 2006; DOI: 10.1007/3 540 34334 2.

(15) Lebas, R.; Menard, T.; Beau, P. A.; Berlemont, A.; Demoulin, F. X. Numerical simulation of primary break up and atomization: DNS and modelling study. *Int. J. Multiph. Flow* **2009**, *35*, 247−260.

(16) Sanjose, M.; Senoner, J.; Jaegle, F.; Cuenot, B.; Moreau, S.; Poinsot, T. Fuel injection model for Euler−Euler and Euler−Lagrange large eddy simulations of an evaporating spray inside an aeronautical combustor. *Int. J. Multiph. Flow* **2011**, *37*, 514−529.

(17) Gjesing, R.; Hattel, J.; Fritsching, U. Coupled atomization and spray modelling in the spray forming process using Openfoam. *Eng. Appl. Comput. Fluid Mech.* **2009**, *3*, 471−486.

(18) Zhou, Z. F.; Lu, G. Y.; Chen, B. Numerical study on the spray and thermal characteristics of R404A flashing spray using Open FOAM. *Int. J. Heat Mass Transf* **2018**, *117*, 1312−1321.

(19) Prosperetti, A.; Tryggvason, G. *Computational Methods for Multiphase Flow*; Cambridge University Press: Cambridge, U.K., 2009.

(20) Yeoh, G. H.; Tu, J. *Computational Techniques for Multiphase Flows*; Butterworth Heinemann: Oxford, U.K., 2019.

(21) Fröhlich, J. *Large Eddy Simulation turbulenter Strömungen*; Teubner Verlag: Berlin, Germany, 2006.

(22) Kärrholm, F. Numerical modelling of diesel spray injection, turbulence interaction and combustion. Ph.D. Thesis, Charlmers University of Technology, Göteborg, Sweden, 2008.

(23) Novella, R.; Garcia, A.; Pastor, J.; Domenech, V. The role of detailed chemical kinetics on CFD diesel spray ignition and combustion modelling. *Math. Comput. Model.* **2011**, *54*, 1706−1719.

(24) Reitz, R. D.; Diwakar, R. Effect of drop breakup on fuel sprays. *SAE Trans.* **1986**, 218−227.

(25) O'Rourke, P. Collective drop effects on vaporizing sprays. Ph.D. Thesis, Princeton University, Princeton, NJ, 1981.

(26) O'Rourke, P. J.; Amsden, A. A spray/wall interaction submodel for the KIVA 3 wall film model. *SAE Trans.* **2000**, 281−298.

(27) Lee, S. Y.; Ryu, S. U. Recent progress of spray wall interaction research. *J. Mech. Sci. Technol.* **2006**, *20*, 1101−1117.